Change of the topology of a superconducting thin film electromagnetically coupled with an array of ferromagnetic nanowires



2016 Supercond. Sci. Technol. 29 015011

(http://iopscience.iop.org/0953-2048/29/1/015011)

IOP Publishing Superconductor Science and Technology
Supercond. Sci. Technol. 29 (2016) 015011 (9pp) doi:10.1088/0953-2048/29/1/015011

# Change of the topology of a superconducting thin film electromagnetically coupled with an array of ferromagnetic nanowires

M Trezza[1], C Cirillo[1], A L Dolgiy[2], S V Redko[2], V P Bondarenko[2], A V Andreyenka[2], A L Danilyuk[2], S L Prischepa[2] and C Attanasio[1]

[1] CNR-SPIN Salerno and Dipartimento di Fisica 'E. R. Caianiello', Università degli Studi di Salerno, via Giovanni Paolo II 132, I-84084 Fisciano (Sa), Italy
[2] Belarusian State University of Informatics and RadioElectronics, P. Brovka street 6, 220013 Minsk, Belarus

E-mail: attanasio@sa.infn.it

Received 30 September 2015, revised 26 October 2015
Accepted for publication 6 November 2015
Published 3 December 2015



**Abstract**

We report on the superconducting properties of a Nb thin film deposited, with an interleaved insulating layer to avoid the proximity effect, on an array of ferromagnetic (Ni) nanowires embedded in a porous template. By investigating the $T_c(H)$ phase boundary and by measuring $V(I)$ characteristics and critical currents as a function of the applied magnetic field, we find that the Nb film exhibits properties similar to those of a network of one-dimensional superconducting nanowires. We attribute this behavior to the stray fields of the magnetic dipoles, which create an almost regular lattice of normal regions in the superconductor, ultimately changing its topology. Furthermore, there is evidence that the magnetic pinning of vortices is negligible in this structure.

Keywords: 1D superconductivity, magnetic nanopillars, porous Silicon, electromagnetically coupled ferromagnetic/superconducting systems

(Some figures may appear in colour only in the online journal)



## 1. Introduction

Superconductivity and ferromagnetism are two competing orderings whose coexistence can be easily achieved in artificial superconductor/ferromagnet (S/F) hybrids [1]. The physics connected to their interaction is rich and interesting and a large number of S/F systems, with or without an insulator (I) between the superconducting and the ferromagnetic layers, have been studied both theoretically and experimentally in the recent years [2–4]. Among the various aspects related to the interplay between superconductivity and magnetism in this kind of structure, magnetic vortex pinning has received considerable interest and has been primarily investigated in systems where arrays of magnetic nanodots interact with a superconducting thin film [5–19]. On the other hand, arrays of ferromagnetic nanowires (NWs) embedded in porous self-assembled templates received considerable interest, due to the possibility to prepare in these structures regular magnetic arrays with characteristic dimensions, i.e., diameter of the wires and nearest neighbor distance, in the nanometer range [20–25]. Self-assembled methods are versatile and reliable techniques, which allow one to quickly fabricate low-cost patterns of nanostructures on very large areas with a high degree of reproducibility. Recently, these systems have been used in conjunction with superconducting films in order to create periodic magnetic pinning centers and study matching effects between the artificial non-superconducting regular structure and the vortex lattice [26–32]. Moreover, this huge experimental activity has also stimulated an intense theoretical analysis of the phenomenon [33–38]. What essentially happens is that, even in the absence of any magnetic field, $H$, the stray fields generated by the magnetic dipoles cause a

 

spatial modulation of the order parameter in the superconducting film. The Cooper pair density is consequently lower in correspondence of the magnetic dots where the order parameter is strongly depressed. Moreover, in the presence of an external field, this causes enhanced pinning when the lattice of superconducting vortices is commensurate with the magnetic dipole array, which is when $H = H_n$. Here, $H_n$ is the so-called $n$th matching field, which is proportional to the magnetic flux quantum $\phi_0$ and whose exact expression is determined by the geometry of the pinning array.

However, in the case of a superconducting film containing a periodic array of non-magnetic nanoholes, it was argued that matching effects can originate from the suppression of the zero-field superconducting critical temperature, $T_{c0}$, rather than from flux pinning enhancement, due to the presence of the holes, which modify the topology of the plain film [39]. In this case, the observed properties of superconducting films with hole arrays [39–42] can be explained in terms of the Little–Parks effect [43], since the system behaves like a superconducting wire network when the superconducting coherence length $\xi$ is of the same order as the width of the channels between the holes $w$. Very recently, this issue has been tackled in the case of ferromagnetic nanodots buried in a superconducting thin film to form an F/S hybrid [44]. It has been established that vortex pinning is, in this case, the main origin of the observed matching effects, while the wire network regime is present only for small magnetic fields and temperatures close to $T_{c0}$, where $\xi(T) \sim w$.

Here we investigate the superconducting properties of a 30 nm thick Nb film sputtered on a dense array of Ni nanowires grown in a nanoporous Si template. Nb is separated from the magnetic dipoles by an insulating $Al_2O_3$ layer to obtain an F/I/S hybrid. By combining magnetoresistance and $V(I)$ characteristics measurements, we establish that the matching effects observed in the Nb film are caused by the Little–Parks effect more than by the vortex pinning, in agreement with theoretical predictions [45, 46]. Therefore, the system behaves like a one-dimensional (1D) superconducting wire network where the confinement of the Cooper pairs is not caused by geometrical constrictions, but rather by the stray fields of the magnetic dipoles that modify the topology of the plain film creating regions where the superconductivity is strongly depressed. Due to the values of $\xi$ and $w$, the wire network behavior is present down to relatively low temperatures and high magnetic fields.

## 2. Experiment

Antimony-doped 100 mm monocrystalline silicon wafers with (100) orientation and 0.01 $\Omega \times$ cm resistivity were used as the initial substrates for porous silicon (PS) formation. Chemical cleaning of the Si wafers was performed for 10 min in a hot (75 °C) solution of $NH_4OH$, $H_2O_2$, and $H_2O$ mixed in a volume ratio of 1:1:4. Later, the wafers were rinsed in deionized water, dried in a centrifuge, and finally cut into rectangular-shaped 3 × 3 $cm^2$ samples. To remove the native oxide, each sample was subsequently immersed into a 5% HF solution for 30 s and then placed into a Teflon electrolytic cell with a 3 $cm^2$ round shape active opening and a platinum spiral wire as a cathode. The uniform PS layer was then formed by electrochemical anodization of a silicon wafer, attached to a spectrally pure graphite disk used as a contact electrode, in a solution of HF (45%), $H_2O$, and $(CH_3)_2CHOH$ mixed in a 1:3:1 volume ratio. The anodization process was performed at a current density of 80 mA $cm^{-2}$ for 200 s that provided the formation of an uniform PS layer 10-$\mu$m thick with 72% of porosity [47]. The pores have an average diameter, $D$, of 80 nm, an average interpore distance (distance between the centers of two consecutive pores), $a_0$, of 120 nm, and density of $6.9 \times 10^9$ $cm^{-2}$, as obtained from scanning electron microscopy (SEM) analyses. The standard deviation of these values of $D$ and $a_0$ is estimated to be around 10% [48]. After the formation of PS, the cell was rinsed in deionized water and then filled with an electrolyte for nickel deposition. Ni was deposited into the PS matrix by electrochemical deposition with a constant 3.5 mA $cm^{-2}$ current density. The electrolyte consisted of 213 g/l $NiSO_4 \times 7H_2O$, 5 g/l $NiCl_2 \times 6H_2O$, 25 g/l $H_3BO_3$, and 3 g/l saccharin. Polyoxyethylene with a high molecular weight was used as an additive to increase the filling factor up to nearly 80%. After 60 min of deposition Ni completely fills the pores and forms a continuous film, approximately 1 $\mu$m thick, on the surface of PS [49]. Finally, Ni was back-sputtered from the surface of the substrate by ion-beam cleaning to leave the ferromagnetic material only inside the pores, where it grows uniformly down to the depth of 8 $\mu$m [49, 50]. Figure 1 shows an SEM image of the PS after the procedure of the Ni filling has been completed. The Curie temperature and the specific magnetization of the arrays of Ni NWs, measured by the ponderomotive method, were close to corresponding values of bulk Ni, i.e., $T = 627$ K and $\sigma = 58.9$ A · $m^2$ $kg^{-1}$, respectively [50]. Moreover, x-ray diffraction patterns revealed the polycrystalline structure of Ni NWs with the preferential orientation along the [111] axis [49, 50]. Figure 2 shows the magnetization hysteresis loops for Ni NWs embedded in the PS template measured at $T = 5$ K with the

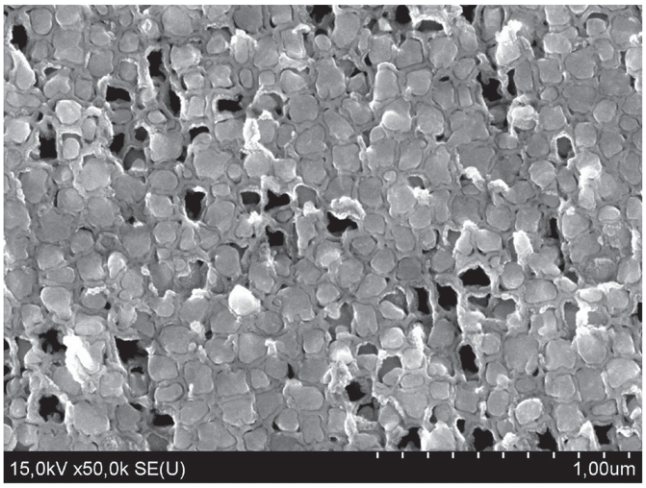


**Figure 1.** SEM top-view image of the array of Ni NWs embedded in the PS template.

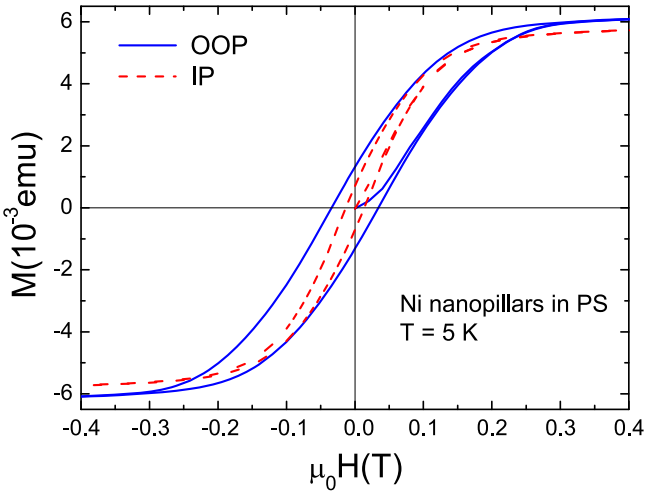


**Figure 2.** Magnetic hysteresis loops for the array of Ni NWs embedded in the PS template at $T = 5$ K in the OOP configuration (continuous blue line) and in the IP configuration (dashed red line).

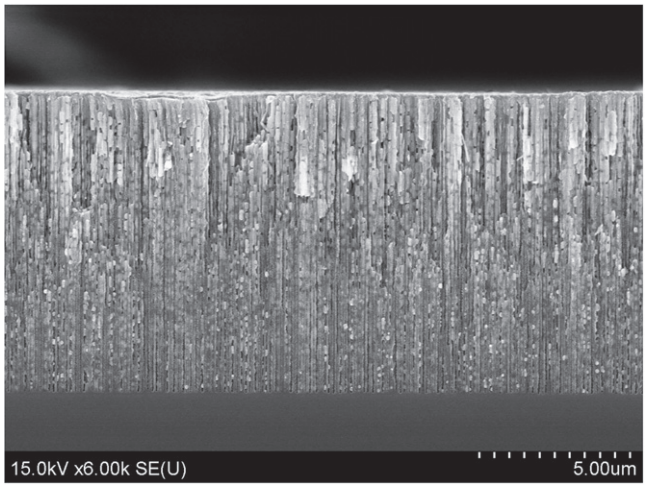


**Figure 3.** SEM cross-section image of sample W.

magnetic field applied either parallel (out-of-plane, OOP) or perpendicular (in-plane, IP) to the Ni NW axis. Measurements were performed in a Quantum Design MPMS XL superconducting quantum interference device (SQUID) magnetometer. Although the IP and OOP magnetization loops are similar, from the figure it can be argued that the sample has the easy axis oriented in the OOP direction (i.e., along the NWs and perpendicular to the plane of the film). We believe that this is mainly due to the strong shape anisotropy of the wires. Since the critical diameter below which Ni nanoparticles become single domain is close to 60 nm [51], it is reasonable to assume that the polycrystalline Ni NWs grown in the 80 nm diameter pores consist of single-domain grains with the magnetization lying along the NW axis.

After the Ni NWs were electrodeposited in the PS templates, a thin insulating layer of $Al_2O_3$ (8 nm thick) was grown by first depositing Al on the PS. Deposition was performed in an UHV dc diode magnetron sputtering, at the rate of 0.014 nm $s^{-1}$, with a base pressure in the low $10^{-8}$ torr regime and a sputtering Ar pressure of $3.75 \times 10^{-3}$ torr. The insulating layer was realized in two steps and between the two consecutive Al depositions the samples were exposed to the atmosphere at the temperature of 100 °C to obtain the formation of the native oxide layer. Finally, Nb thin films were grown in the same sputtering system using an Ar pressure of $2.6 \times 10^{-3}$ torr, at the rate of 0.33 nm $s^{-1}$. The sample under investigation is a Nb film of thickness $d = 30$ nm (sample W). Due to the presence of the insulating buffer layer between the superconductor and the PS filled with the Ni nanopillars, the system under study is an F/I/S hybrid. In this way, the proximity effect and exchange of electrons are completely avoided and the interaction between the superconducting and the ferromagnetic systems is totally electromagnetic. A reference sample (sample F) was also prepared and analyzed. It was fabricated by depositing a continuous 1 $\mu$m thick Ni layer onto a PS template. Subsequently, the $Al_2O_3$ and the Nb layers were grown exactly as described previously. An SEM cross-section image of sample W is shown in figure 3.

Superconducting electric transport properties were measured in a $^4$He cryostat using a standard dc four-probe technique. The samples were unpatterned and contacts put in-line. The width of sample W (sample F) was equal to 3 mm (5 mm). The distance between the current (voltage) pads was less than 6 mm (1 mm), both in sample W and sample F. A dc excitation current of 0.1 mA was used to bias the samples. The external magnetic field was always applied perpendicularly to the plane of the film and to the direction of the flowing current. The superconducting transition temperature of the samples in the absence of applied field has been taken as the temperature at which the resistance is equal to 50% of the normal state resistance $R_N$. It was $T_{c0} = 5.0$ K ($T_{c0} = 5.5$ K) for sample W (sample F). *I–V* characteristics were recorded using a pulsed technique [52]. Before starting the measurements, the Ni NWs were first magnetized at low temperatures in a perpendicular magnetic field of 1 T which, as can be seen from figure 2, is far above the saturation field of Ni NWs.

From the measured low-temperature value of the normal state resistivity of the Nb film, $\rho(T = 10\ K) = 18\ \mu\Omega$ cm, since for Nb it is [53] $\rho\ell = 3.72 \times 10^{-6}\ \mu\Omega\text{cm}^2$, we estimate a mean free path of $\ell = 2$ nm. The Ginzburg–Landau coherence length $\xi(T) = \xi(0)/\sqrt{1 - T/T_{c0}}$ and the magnetic field penetration depth $\lambda(T) = \lambda(0)/\sqrt{1 - T/T_{c0}}$ can be found at any temperature using for $\xi(0)$ and $\lambda(0)$ the dirty limit expressions [54] (valid when $\ell < \xi_0$) $\xi(0) = 0.85(\xi_0\ell)^{1/2}$ and $\lambda(0) = 0.66\lambda_0(\xi_0/\ell)^{1/2}$. $\xi_0 = 38$ nm [55] and $\lambda_0 = 39$ nm [55] are the values for the BCS coherence length and the London penetration depth of Nb, respectively. Therefore, we have $\xi(0) = 7.4$ nm and $\lambda(0) = 100$ nm. As a consequence, the Ginzburg–Landau parameter is $\kappa = \lambda(0)/\xi(0) = 12$ and therefore the sample is a type-II superconductor.

## 3. Results and discussion

Figure 4(a) shows the $T_c(H)$ phase diagram constructed by measuring resistive transitions in various perpendicular magnetic fields for sample W. The three curves have been

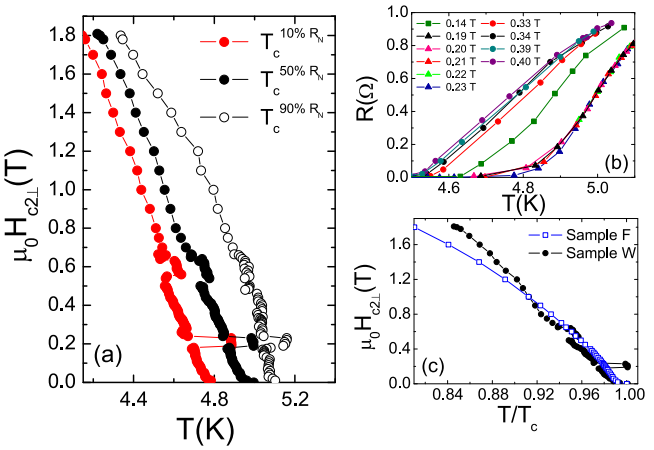


**Figure 4.** (a) $T_c(H)$ phase diagrams of sample W obtained with resistive criteria of 10%, 50%, and 90% of $R_N$, the normal state resistance. (b) Resistive transitions of sample W for a selection of applied fields. The curves from 0.19–0.23 T (at 0.14 T and from 0.33–0.40 T) are representative of the temperature dependence of the resistance at fields where the bump is (is not) present in the phase diagram. (c) *H*–*T* phase diagrams of the samples W and F, both obtained with the 50% of $R_N$ criterion.

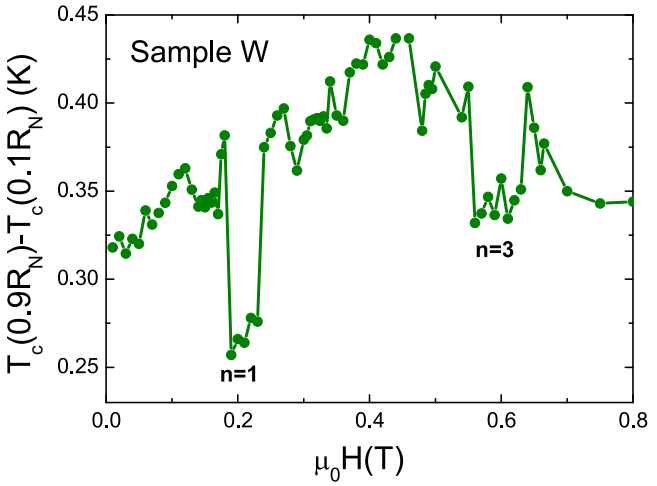


**Figure 5.** Transition width $T_c(90\%\ R_N) - T_c(10\%\ R_N)$ of the $R(T)$ curves for sample W as a function of $H$. $n = 1$ ($n = 3$) is the integer labelling the first (third) matching field.

obtained using different resistive transition criteria of the normal state resistance, namely 10%, 50%, and 90% of $R_N$. The phase boundary shows a pronounced anomaly in the field range 0.19–0.23 T where the critical temperature apparently increases with respect to what is conventionally expected, reaching a value that is almost equal to $T_{c0}$. The bump is also present at higher fields, in the range 0.53–0.64 T, though with a lower amplitude. Furthermore, the amplitude of the two bumps decreases when a higher resistance criterion is adopted, consistently with previous observations in similar systems [39, 41–43, 56]. In particular, the anomaly present at higher fields is smeared out when the criterion of 90% of $R_N$ is adopted [open circles in figure 4(a)]. A selection of the $R(T)$ curves in different fields is shown in figure 4(b). In figure 4(c) the phase boundary of the control sample F, constructed with the criterion of 50% of $R_N$, is compared with the one of sample W, obtained using the same resistive criterion. We see that the curve is smooth and does not show any anomalous feature. Moreover, the critical field of sample W is not substantially enhanced over the investigated temperature range with respect to the critical field of the reference plain Nb film. This could be a first indication about the marginal role played by magnetic pinning in this sample [57]. However, if the holes in PS (and consequently the Ni NWs) are supposed to be arranged in a triangular lattice, as it is typically the case for self-assembled templates [41], the matching fields are given by $H_n = nH_m = n \times 1.15(\phi_0/a_0^2)$, where $n \geqslant 1$ is an integer and $\phi_0 = 2.07 \times 10^{-15}\ T\ m^2$ is the flux quantum. Interestingly, if we take $H_1 = 2$ kOe, a value of field falling in the range where the first apparent increase of $T_c$ is observed in the phase boundary, we obtain $a_0 = 109$ nm, which is very close to the nominal value of 120 nm for the average interpore distance. Moreover, $H_3 = 3H_1 = 6$ kOe a value that falls almost in the middle of the range of fields where the second anomaly is present in the phase diagram. The bump is not observed for fields around $H_2 = 4$ kOe. At the moment, we do not have a clear explanation of why the phase boundary of sample W is smooth and does not present any relevant feature at $H = H_2$.

It is also worth noticing that the superconducting transition curves shown in figure 4(b) are parallel in each of the considered field intervals. The five curves belonging to the field interval 0.19–0.23 T, where the first bump in the phase diagram is present, essentially overlap and develop a tail in the lower part of the curve, below 10% of $R_N$. To better analyze this effect, figure 5 shows the $R(T)$ transition width $T_c(90\%\ R_N) - T_c(10\%R_N)$ as a function of $H$ for all the $R(T)$ transitions. The broadening shows an abrupt decrease at both the field intervals that contain the matching fields $H_1$ and $H_3$.

The critical current, $I_c$, of sample W is shown in the main panel of figure 6 as a function of the magnetic field for $T = 2.64$ K, corresponding to temperature $T = 0.53\ T_{c0}$. The critical current shows a monotonous behavior and, apart from a very tiny increase for fields around 6 kOe, it does not present any feature that can be related to the presence of the array of Ni NWs, also for fields around 2 kOe, where the large bump was observed in the $T_c(H)$ phase diagram. Indeed, the same field dependence is exhibited by the critical current of the control sample (sample F), as can be seen in inset (a) of figure 6 where $I_c(H)$, measured at $T = 4.0$ K i.e., at $T = 0.73\ T_{c0}$, is plotted. For both samples, $I_c$ was defined by the voltage criterion of $V_c = 1\ \mu$V, corresponding to the electric field criterion of $E_c = 10^{-5}\ \mathrm{V\,cm^{-1}}$. The comparison between the two curves indicates that the array of magnetic pinning sites does not considerably influence the field dependence of the critical current, which, on the contrary, is mainly determined by the random (and stronger) pinning centers present in the superconducting film. This is consistent with other results reported in the literature [13], where it has also been noticed that, in order to observe the increase of the $I_c(H)$ curve at matching fields, larger and/or perforating magnetic dots are needed [7, 10]. Coherently, if the critical

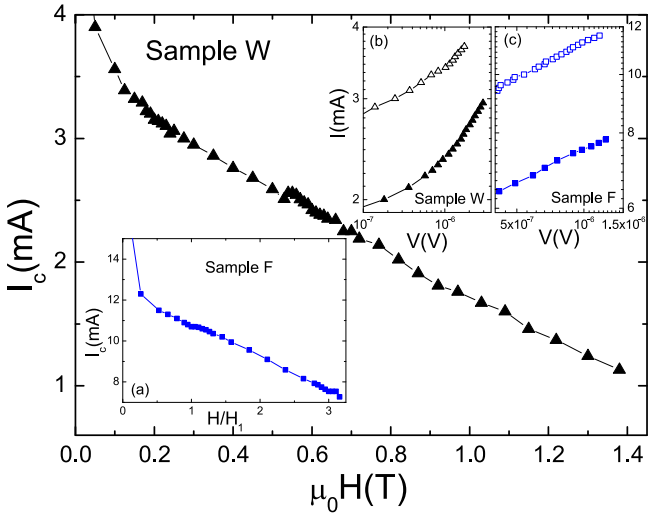


**Figure 6.** Magnetic field dependence of the critical current of sample W at $T = 0.53\ T_{c0}$ ($T = 2.64$ K). Insets: (a) magnetic field dependence of the critical current of sample F at $T = 0.73\ T_{c0}$ ($T$=4.0 K). The field has been normalized to $H_1 = 2$ kOe. (b) $I$–$V$ characteristics for sample W at and away from the third matching field and at $T = 0.53\ T_{c0}$. Closed (open) triangles are for $H = 6$ kOe ($H = 1.25$ kOe). (c) $I$–$V$ characteristics for sample F at $T = 0.73\ T_{c0}$ and $H = 6$ kOe ($H = 1.25$ kOe), closed (open) squares.

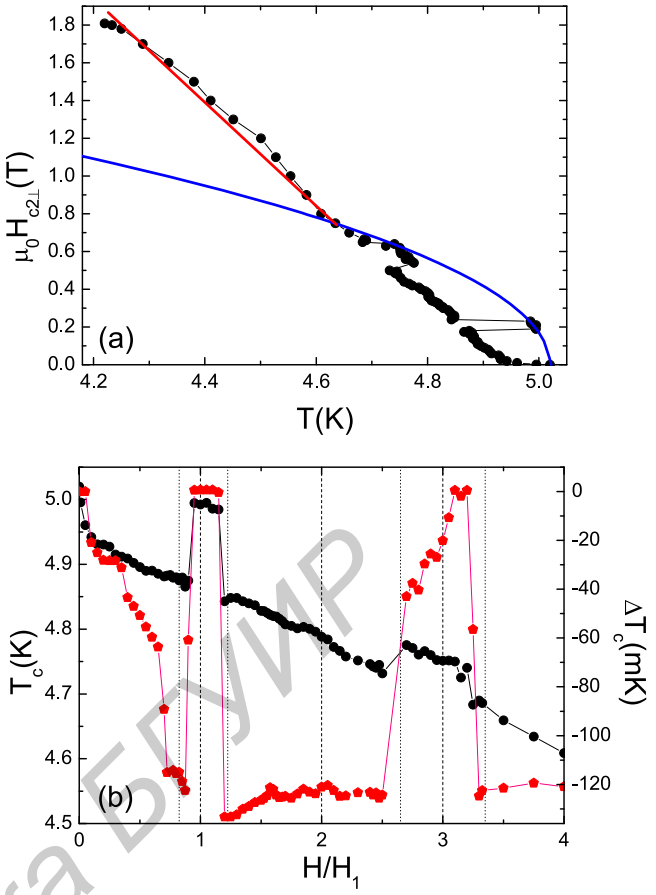


**Figure 7.** (a) Upper critical field of sample W derived with the resistive criterion of 50% of $R_N$. The blue line represents the parabolic 1D fit to the maxima in the $T_c(H)$ curve. The red line is a guide to the eye to show the nearly linear behavior of the phase diagram below $T = 4.6$ K. (b) On the left axis the superconducting phase diagram of sample W in the $H/H_1$–$T_c$ plane is shown (black circles). The magnetic field is normalized to the first matching field, $H_1 = 2$ kOe. Vertical dashed lines indicate multiples of the first matching field. Vertical dotted lines indicate the matching fields calculated in correspondence of $a_0 \pm 0.1\ a_0$, both for $n = 1$ and for $n = 3$. The right axis (red pentagons) shows $\Delta T_c(H)$, which is defined as the difference between the experimental $T_c$ values and those obtained from the 1D fit, both reported in panel (a).

current density, $J_c$, is roughly estimated considering the geometrical dimensions of the two samples, it results in both cases of the same order of magnitude. For example, at low fields, for sample W it is $J_c \approx 4.4 \times 10^7$A m$^{-2}$ at $T = 0.53\ T_{c0}$, while for sample F, even at higher reduced temperature, $T = 0.73\ T_{c0}$, it is $J_c \approx 1 \times 10^8$A m$^{-2}$. Inset (b) of figure 6 presents two $V(I)$ characteristics for sample W measured at $T = 0.53\ T_{c0}$, one at the third matching field $H_3 = 6$ kOe and the other far from it (at $H = 1.25$ kOe). The curves have same shape, indicating that the same vortex phase is present at and out of the matching conditions. For comparison, we measured $V(I)$ curves for sample F at the same magnetic fields. Inset (c) of figure 6 displays data taken at $T = 0.73\ T_{c0}$. The aspect of these two curves is similar and, more interestingly, it is not dramatically different from those shown for sample W. Also, this last evidence corroborates the conjecture that the underlying array of Ni NWs does not appreciably modify the pinning mechanism in the Nb film.

The previous data show that magnetic pinning does not play a relevant role in the system under study, so the observed anomalies in the superconducting phase diagram can be hardly ascribed to pinning enhancement due to the presence of the array of Ni NWs. On the other hand, the stray fields of the magnetic dipoles oriented perpendicularly to the plane of the film can create normal zones in the sample [36, 58, 59], which have the same arrangement of the underlying lattice of ferromagnetic NWs. The numerical simulations reported in the appendix and obtained using a magnetostatic model explicitly show that this condition is realized for the system under study. As a result, the topology of the plain Nb film is changed and the system is a virtual network of superconducting channels (the regions where the density of Cooper pairs is high) flowing around zones where, on the contrary, the superconducting order parameter practically vanishes. Therefore, these regions can be considered as equivalent to dots or antidots in a superconducting film and their presence causes a change in the temperature dependence of the perpendicular critical field $H_{c2}(T)$ [39, 60–62]. For temperatures near $T_{c0}$, the phase boundary has an oscillatory behavior where the maxima in the critical temperature follow a parabolic law obtained from the expression $H_{c2}(T) = \sqrt{3}\,\phi_0/[\pi w \xi(T)] = \sqrt{3}\,\phi_0/[\pi w \xi(0)(1 - T/T_{c0})^{-1/2}]$ [40, 63]. This behavior, which is typical of a 1D superconducting wire network, occurs when $1.84\xi(T) \geqslant w$ [64].

Figure 7(a) shows the $T_c(H)$ curve of sample W obtained with the resistive criterion of 50% of $R_N$ together with the 1D parabolic fit to the data (blue curve). The fit, which has been performed fixing $\xi(0) = 7.4$ nm as calculated previously from low-temperature resistivity measurements, yields for the

lateral width of the superconducting channels a value of $w = 53$ nm. For $T \lesssim 4.6$ K ($T \lesssim 0.92\ T_{c0}$) the phase diagram develops a nearly linear behavior, which is characteristic of a continuous two-dimensional superconducting film in perpendicular magnetic field in the considered temperature range. Because vortices will preferably enter the zones of the film where the superconductivity is depressed by the stray fields, we can consider $w \approx a_0 - 2\xi(T)$, being $2\xi(T)$ the dimension of the vortices at a certain temperature. At $T$=4.75 K, in the middle of the range where anomalies in the $H_{c2}(T)$ were observed, it is $w \approx 54$ nm, which is in perfect agreement with the result of the fitting procedure. Furthermore, since in our case it is $w \approx 54$ nm, the condition to observe the Little–Parks effect is fulfilled for $T \gtrsim 4.67$ K, once again in nice correspondence with the experimental behavior observed for $H_{c2}(T)$. Moreover, the irregularity of the arrangement of the normal zones in the Nb film can be responsible for the observation that the $T_c(H)$ phase diagram exhibits, rather than well-defined maxima at matching fields, a broad field interval where the critical temperature is not suppressed. Because the distribution in the values of $a_0$ is estimated to be around 10% of the nominal value in our PS template [48], it is reasonable to assume that the lower and upper bounds of the field intervals where the Little–Parks effect is present can be calculated in correspondence of $a_0 \pm 0.1a_0$, respectively. Even with this rough hypothesis, the field interval that displays the Little-Parks effect is well reproduced for both $H_1$ and $H_3 = 3H_1$, as shown by vertical dotted lines in figure 7(b), left axis. The magnetic field dependence of the variation of the critical temperature, $\Delta T_c(H)$, calculated as the difference between the experimental values and those obtained from the 1D parabolic fit to the data, is displayed in figure 7(b), right axis. $\Delta T_c(H)$ does not show a true oscillatory behavior, as theoretically predicted [63] and experimentally observed in superconducting films containing regular arrays of dots [44] or antidots [40, 42]. Again, this can be due to actual arrangement of the normal regions in the superconducting film. Moreover, a very strong suppression of $T_c$ is observed for magnetic fields different from the matching values. From the theory, for a thin superconducting ring of diameter $D$ in the dirty limit, it is [63] $\Delta T_c(H) = -T_{c0}[(2.92\xi_0\ell)/D^2](n - \phi/\phi_0)^2$, where the integer $n = 0, 1, 2,...$, and $\phi$ is flux per unit cell. For the sample W, the expected value of the amplitude of the $T_c(H)$ oscillations is $\Delta T_c^{\rm th} = 43$ mK, while the experimental value found for the maximum amplitude is $\Delta T_c^{\rm exp} \approx 130$ mK, a factor of three larger. This observation is consistent to what was obtained for a regular structure consisting of a ferromagnetic particle array deposited on a Nb layer, because no real holes are present in the Nb film but only in regions where the superconductivity is depressed [65]. A disagreement between theory and experiment for the amplitude of $\Delta T_c$ was also recently reported for a similar system [44]. On the other hand, in that case, it was $\Delta T_c^{\rm th} > \Delta T_c^{\rm exp}$, an experimental finding that was attributed to the relevant role of vortex pinning in the sample, which decreased the Little–Parks oscillations [44].

## 4. Conclusions

In conclusion, robust nanoporous Si templates have been used to host a dense array of electrodeposited Ni NWs that electromagnetically interact with a Nb thin film to form an F/I/S hybrid. We have observed strong anomalies in the $T_c(H)$ superconducting phase boundary, which are not caused by matching effects between the array of NWs and the vortex lattice, but rather, they are related to the Little–Parks effect. The main role of the array of magnetic NWs is not to enhance pinning of superconducting vortices but to cause a change in the topology of the film. This is done by creating a physical network of narrow superconducting zones that develop around regions where the superconducting order parameter, due to the stray fields of the Ni nanowires, is strongly depressed. The presence of these regions determines an additional depression of the critical temperature at fields different from the matching fields. Importantly, due to the values of $\xi$ and $w$, the studied system mimics a 1D superconducting wire network down to $T \sim 0.92\ T_{c0}$ in fields as high as 6 kOe. The analyzed F/I/S system, even though not very highly ordered, can be conveniently used to obtain a network of 1D superconducting nanowires in the presence of a magnetic array, with the advantage of depositing the superconducting film on a smooth buffer layer instead of an irregular porous template. This implies that, for example, resistivity will be smaller and, consequently, $\xi(0)$ larger in such a way to obtain the condition for the realization of a 1D superconducting wire network in a larger temperature range. In the next future, using electron beam lithography (EBL), we plan to fabricate analogous systems with a much smaller number of interconnected nanowires (∼50) in order to observe quantum phase slip related phenomena [66], as already studied in Nb ultra-thin films deposited on PS templates [67–69].



## Acknowledgments

The authors wish to thank A A Maximenko for magnetic measurements.

## Appendix

The magnetic field profile in the Nb due to the array of Ni nanopillars has been calculated using a magnetostatic model. The array has been modelled considering nine single-domain Ni cylinders 800 nm height, arranged in a square-lattice configuration and embedded in pure silicon. Each cylinder has a diameter of 80 nm while the center-to-center distance between two nearest pillars is 120 nm. The presence of the very thin insulating layer of $Al_2O_3$ has been neglected in the calculations. Finally, the array was covered on the top by a 30 nm Nb layer and closed from the bottom by a 100 nm Si layer. We have verified that if the nanopillars' height is increased above 800 nm, while calculations become quite time-consuming, the results of the simulations do not

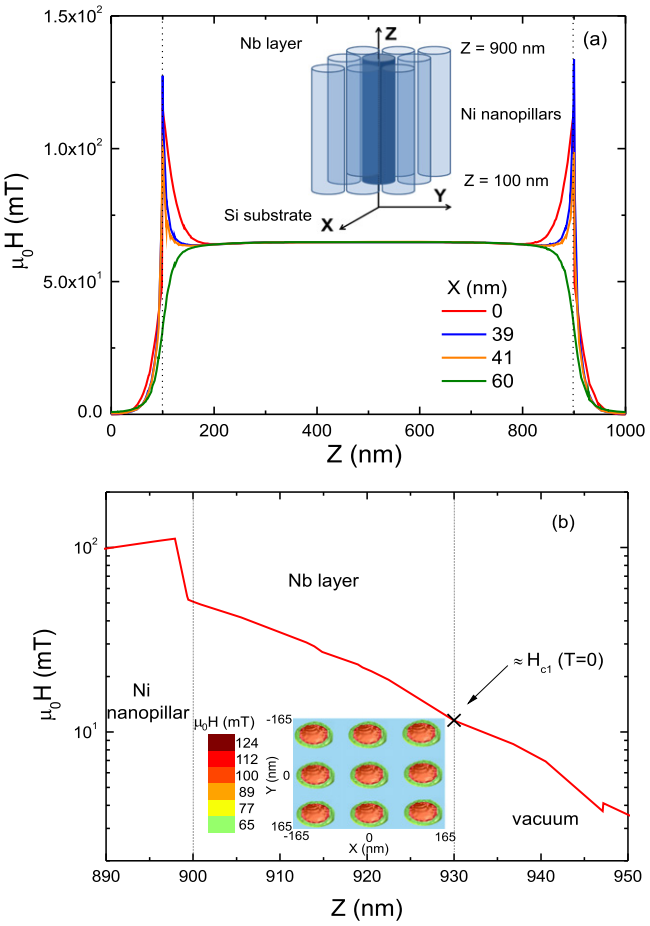


**Figure 8.** (a) The magnetic field profile due to the central Ni nanopillar of the array, evaluated for different values of the $x$ coordinate. The inset illustrates the schematic drawing of the array. (b) The magnetic field profile in the Nb layer due to the central Ni nanopillar, evaluated for $x = 0$. The two vertical lines mark the $z$ coordinates where the external surfaces of the Nb film are positioned. The cross indicates the zero temperature $H_{c1}$ value for the Nb film. The contour plot shows the $x$–$y$ distribution of the magnetic field at the upper surface of the Ni nanopillars, calculated using a magnetostatic model.

significantly change. A schematic representation of the investigated structure is shown in the inset of figure 8(a).

We started from the Maxwell equations for the magnetic field, **H**, and the magnetic induction, **B**, in the current free region

$$\nabla \times \mathbf{H} = 0 \tag{1}$$

and

$$\nabla \times \mathbf{B} = 0 \tag{2}$$

Since in this case the stationary magnetic field is vortex free, it can be described by a scalar magnetic potential, $V_m$. In this way, the spatial distribution of **H** can be obtained by solving the equation

$$\mathbf{H} = -\nabla V_m \tag{3}$$

When the magnetization curve is obtained, as in our case, starting from zero field, the relation between **H** and **B** is given, for a system of permanent magnets, by

$$\mathbf{B} = \mu_0 \mu \mathbf{H} + \mathbf{B}_{\text{rem}} \tag{4}$$

where $\mathbf{B}_{\text{rem}} = \mu_0 \mathbf{M}_{\text{rem}}$ is the remanent induction of the material, $\mu_0$ is the magnetic constant, and $\mu$ is the relative permeability of the medium. Therefore, the equation for the magnetic field is

$$-\nabla \cdot \left(\mu \mu_0 \nabla V_m - \mu_0 \mathbf{M}_{\text{rem}}\right) = 0 \tag{5}$$

To be solved, equations (4) and (5) should be supplemented by the appropriate boundary conditions. We put the main axis of the nanopillars along the $z$ direction, see inset of figure 8(a). The magnetic field is then tangential to the $z$ direction and the boundary conditions read as

$$\mathbf{n} \cdot \left(\mu \mu_0 \nabla\left(V_m\right) - \mu_0 \mathbf{M}_{\text{rem}}\right) = \mathbf{n} \cdot \mathbf{B} = 0 \tag{6}$$

where, **n** is the $z$ axis versor. For the magnetic field components in the $x$–$y$ plane a constant magnetic scalar potential has been assumed which, for the sake of convenience, was taken equal to zero. On the basis of the preceding equations, the magnetic field and its space distribution were calculated numerically using the package COMSOL Multiphysics. The main panel of figure 8(a) shows the magnetic field profile in correspondence with the central Ni cylinder in the square array obtained from the preceding equations by using $\mu_0 M_{\text{sat}} = 616$ mT for the saturation magnetization of the Ni nanopillars, value measured for the bulk material [50], and $\mu_0 M_{\text{rem}} = 166$ mT for the remanence. This last value has been calculated from the squareness $Sq$ of the hysteresis loop shown in figure 2, for which $Sq$=0.27. For the relative permeability values we took: $\mu_{\text{vacuum}} = \mu_{\text{Si}} = \mu_{\text{Nb}} = 1$ and $\mu_{\text{Ni}} = 600$. The different curves refer to different values of the $x$ coordinate: i.e., at the center of the nanopillar, $x = 0$ (red line), at the inner border of the nanopillar, $x = 39$ nm (blue line), at the outer border of the nanopillar, $x = 41$ nm (orange line), and outside the nanopillar, halfway through the center-to-center distance of two adjacent nanopillars, $x = 60$ nm (green line). The vertical dashed lines indicate the $z$ coordinates where the two bases of the cylinder are located. We see that the magnetic field profile has its maximum value close to the boundaries of the nanopillar. The largest field on the upper face of the nanopillar ($z = 900$) is at $x = 39$ nm but the difference between this value and the value at $x = 0$ nm is very small, i.e., about only 10%. To further clarify this point, in the inset of figure 8(b) we plot the distribution in the $x$-$y$ plane of the $z$ component of the magnetic field of the array of the nine nanopillars evaluated at $z = 900$ nm. The graph shows that the field is almost constant on the outer surface of the nanopillars. A magnification of the result obtained at $x = 0$ (red curve in panel (a)) is shown in the main panel of figure 8(b) for $z$ in the range 890–950 nm. The two vertical lines mark the limits of the Nb film. On the Nb outer surface the magnetic field is approximately 10 mT, number which is considerably close to the zero temperature $H_{c1}$ value estimated for our Nb film [70]. This result supports the idea that the remanence of Ni nanopillars has a strong influence on

the superconducting properties of the Nb film at temperatures close to $T_c$, where $H_{c1}$ is much smaller than 10 mT.

## References


[1] Buzdin A I 2005 Proximity effects in superconductor-ferromagnet heterostructures *Rev. Mod. Phys.* **77** 935–76

[2] Lyuksyutov I F and Pokrovsky V L 2005 Ferromagnet-superconductor hybrids *Adv. Phys.* **54** 67–136

[3] Vélez M, Martín J I, Villegas J E, Hoffmann A, González E M, Vicent J L and Schuller I K 2008 Superconducting vortex pinning with artificial magnetic nanostructures *J. Magn. Magn. Mater.* **320** 2547–62

[4] Aladyshkin A Yu, Silhanek A V, Gillijns W and Moshchalkov V V 2009 Nucleation of superconductivity and vortex matter in superconductor-ferromagnet hybrids *Supercond. Sci. Technol.* **22** 053001

[5] Martín J I, Vélez M, Nogués J and Schuller I K 1997 Flux pinning in a superconductor by an array of submicrometer magnetic dots *Phys. Rev. Lett.* **79** 1929–32

[6] Jaccard Y, Martín J I, Cyrille M C, Vélez M, Vicent J L and Schuller I K 1998 Magnetic pinning of the vortex lattice by arrays of submicrometric dots *Phys. Rev.* B **58** 8232–5

[7] Morgan D J and Ketterson J B 1998 Asymmetric flux pinning in a regular array of magnetic dipoles *Phys. Rev. Lett.* **80** 3614–7

[8] Terentiev A, Watkins D B, De Long L E, Morgan D J and Ketterson J B 1999 Observation of magnetic flux pinning in a thin Nb film with a square lattice of nickel dots *Physica* C **324** 1–8

[9] Martín J I, Vélez M, Hoffmann A, Schuller I K and Vicent J L 1999 Artificially Induced Reconfiguration of the vortex lattice by arrays of magnetic dots *Phys. Rev. Lett.* **83** 1022–5

[10] Hoffmann A, Prieto P and Schuller I K 2000 Periodic vortex pinning with magnetic and nonmagnetic dots: The influence of size *Phys. Rev.* B **61** 6958–65

[11] Martín J I, Vélez M, Hoffmann A, Schuller I K and Vicent J L 2000 Temperature dependence and mechanisms of vortex pinning by periodic arrays of Ni dots in Nb films *Phys. Rev.* B **62** 9110–6

[12] Van Bael M J, Bekaert J, Temst K, Van Look L, Moshchalkov V V, Bruynseraede Y, Howells G D, Grigorenko A N, Bending S J and Borghs G 1999 Local observation of field polarity dependent flux pinning by magnetic dipoles *Phys. Rev. Lett.* **86** 155–8

[13] Vélez M, Jaque D, Martín J I, Guinea F and Vicent J L 2002 Order in driven vortex lattices in superconducting Nb films with nanostructured pinning potentials *Phys. Rev.* B **65** 094509

[14] Villegas J E, Gonzalez E M, Montero M I, Schuller I K and Vicent J L 2005 Vortex-lattice dynamics with channeled pinning potential landscapes *Phys. Rev.* B **72** 064507

[15] Villegas J E, Gonzalez E M, Sefrioui Z, Santamaria J and Vicent J L 2005 Vortex phases in superconducting Nb thin films with periodic pinning *Phys. Rev.* B **72** 174512

[16] Silhanek A V, Gillijns W, Milošević M V, Volodin A, Moshchalkov V V and Peeters F M 2008 Optimization of superconducting critical parameters by tuning the size and magnetization of arrays of magnetic dots *Phys. Rev.* B **76** 100502(R)

[17] Hoffmann A, Fumagalli L, Jahedi N, Sautner J C, Pearson J E, Mihajlović G and Metlushko V 2008 Enhanced pinning of superconducting vortices by magnetic vortices *Phys. Rev.* B **77** 060506(R)

[18] Rosen Y J, Sharoni A and Schuller I K 2010 Enhanced superconducting vortex pinning with disordered nanomagnetic arrays *Phys. Rev.* B **82** 014509

[19] Gomez A, Gilbert D A, Gonzalez E M, Liu K and Vicent J L 2013 Control of dissipation in superconducting films by magnetic stray fields *Appl. Phys. Lett.* **102** 052601

[20] Zeng H, Zheng M, Skomski R, Sellmyer D J, Liu Y, Menon L and Bandyopadhyay S 2000 Magnetic properties of self-assembled Co nanowires of varying length and diameter *J. Appl. Phys.* **87** 4718–20

[21] Zheng M, Menon L, Zeng H, Liu Y, Bandyopadhyay S, Kirby R D and Sellmyer D J 2000 Magnetic properties of Ni nanowires in self-assembled arrays *Phys. Rev.* B **62** 12282–6

[22] Nielsch K, Wehrspohn R B, Barthel J, Kirschner J, Gösele U, Fischer S F and Kronmüller H 2001 Hexagonally ordered 100 nm period nickel nanowire arrays *Appl. Phys. Lett.* **79** 1360–2

[23] Martín J I, Nogués J, Liu K, Vicent J L and Schuller I K 2003 Ordered magnetic nanostructures: Fabrication and properties *J. Magn. Magn. Mater.* **256** 449–501

[24] Sellmyer D J, Zheng M and Skomski R 2001 Magnetism of Fe, Co and Ni nanowires in self-assembled arrays *J. Phys.: Condens. Matter* **13** R433–60

[25] Ye Z, Liu H, Luo Z, Lee H, Wu W, Naugle D G and Lyuksyutov I 2009 Thickness dependence of the microstructures and magnetic properties of electroplated Co nanowires *Nanotechnology* **20** 045704

[26] Hallet X, Mátéfi-Tempfli M, Michotte S, Piraux L, Vanacken J, Moshchalkov V V and Mátéfi-Tempfli S 2009 High magnetic field matching effects in NbN films induced by template grown dense ferromagnetic nanowires arrays *Appl. Phys. Lett.* **95** 252503

[27] Kim K, Ozmetin A E, Naugle D G and Lyuksyutov I F 2010 Flux pinning with a magnetic nanorod array *Appl. Phys. Lett.* **97** 042501

[28] Lyuksyutov I F 2010 Magnetic nanorod-superconductor hybrids *J. Supercond. Nov. Magn.* **23** 1047–9

[29] Ye Z, Naugle D G, Wu W and Lyuksyutov I 2010 Superconducting Properties of Pb/Bi Films Quench-Condensed on a Porous Alumina Substrate Filled with Co Nanowires *J. Supercond. Nov. Magn.* **23** 1083–5

[30] Hallet X, Adam S, Piraux L, Vanacken J and Moshchalkov V V 2011 Superconducting properties of perforated NbN films using ordered arrays of ferromagnetic nanowires *Phys. Rev.* B **84** 144529

[31] Ye Z, Lyuksyutov I F, Wu W and Naugle D G 2011 Superconducting properties of $Pb_{82}Bi_{18}$ films controlled by ferromagnetic nanowire arrays *Supercond. Sci. Technol.* **24** 024019

[32] Trezza M, Cirillo C, Vorobjeva A I, Outkina E A, Prischepa S L and Attanasio C 2013 Vortex matching effects in Nb thin films due to Ni nanopillars embedded in anodic aluminum oxide substrates *Supercond. Sci. Technol.* **26** 035001

[33] Lyuksyutov I F and Pokrovsky V 1999 Magnetization Controlled Superconductivity in a Film with Magnetic Dots *Phys. Rev. Lett.* **81** 2344–7

[34] Erdin E, Kayali A F, Lyuksyutov I F and Pokrovsky V L 2002 Interaction of mesoscopic magnetic textures with superconductors *Phys. Rev.* B **66** 014414

[35] Milošević M V, Yampolskii S V and Peeters F M 2002 Magnetic pinning of vortices in a superconducting film: The antivortex-magnetic dipole interaction energy in the London approximation *Phys. Rev.* B **66** 174519

[36] Priour D J Jr and Fertig H A 2004 Vortex states of a superconducting film from a magnetic dot array *Phys. Rev. Lett.* **93** 057003

[37] Erdin S 2005 London study of vortex states in a superconducting film due to a magnetic dot *Phys. Rev.* B **72** 014522
[38] Milošević M V and Peeters F M 2005 Field-enhanced critical parameters in magnetically nanostructured superconductors *Europhys. Lett.* **70** 670–6
[39] Patel U, Xiao Z L, Hua J, Xu T, Rosenmann D, Novosad V, Pearson J, Welp U, Kwok W K and Crabtree G W 2007 Origin of the matching effect in a superconducting film with a hole array *Phys. Rev.* B **76** 020508(R)
[40] Welp U, Xiao Z L, Jiang J S, Vlasko-Vlasov V K, Bader S D, Crabtree G W, Liang J, Chik H and Xu J M 2002 Superconducting transition and vortex pinning in Nb films patterned with nanoscale hole arrays *Phys. Rev.* B **66** 212507
[41] Luo Q, Zeng X Q, Miszczak M E, Xiao Z L, Pearson J, Xu T and Kwok W K 2012 Phase slippage driven dissipation and high-field Little-Parks effect in superconducting MoGe nanowire networks formed on nanoporous substrates *Phys. Rev.* B **85** 174513
[42] Latimer M L, Xiao Z L, Hua J, Joshi-Imre A, Wang Y L, Divan R, Kwok W K and Crabtree G W 2013 Anisotropy of the critical temperature of a superconducting niobium thin film with an array of nanoscale holes in an external magnetic field *Phys. Rev.* B **87** 020507(R)
[43] Parks R D and Little W A 1964 Fluxoid quantization in a multiply-connected superconductor *Phys. Rev.* **133** A97–103
[44] Gomez A, del Valle J, Gonzalez E M, Chiliotte C E, Carreira S J, Bekeris V, Prieto J L, Schuller I K and Vicent J L 2014 Vortex pinning vs superconducting wire network: Origin of periodic oscillations induced by applied magnetic fields in superconducting films with arrays of nanomagnets *Supercond. Sci. Technol.* **27** 065017
[45] Aladyshkin A Yu, Mel'nikov A S and Ryzhov D A 2003 The Little-Parks effect and multiquanta vortices in a hybrid superconductor-ferromagnet system *J. Phys: Condens. Matter* **15** 6591–7
[46] Aladyshkin A Yu, Ryzhov D A, Samokhvalov A V, Savinov D A, Mel'nikov A S and Moshchalkov V V 2007 Localized superconductivity and Little-Parks effect in superconductor/ferromagnet hybrids *Phys. Rev.* B **75** 184519
[47] Dolgiy A, Bandarenka H, Prischepa S, Yanushkevich K, Nenzi P, Balucani M and Bondarenko V 2012 Electrochemical deposition of Ni into mesoporous silicon *ECS Trans.* **41** 111–8
[48] Trezza M *et al* 2008 Superconducting properties of Nb thin films deposited on porous silicon templates *J. Appl. Phys.* **104** 083917
[49] Dolgiy A, Redko S V, Bandarenka H, Prischepa S L, Yanushkevich K, Nenzi P, Balucani M and Bondarenko V 2012 Electrochemical deposition and characterization of Ni in mesoporous silicon *J. Electrochem. Soc.* **159** D623–7
[50] Dolgiy A L, Redko S V, Komissarov I, Bondarenko V P, Yanushkevich K I and Prischepa S L 2013 Structural and magnetic properties of Ni nanowires grown in mesoporous silicon templates *Thin Solid Films* **543** 133–7
[51] Chernavskij P A 2002 New in magnetic methods of investigations of metal-deposited catalysts *Russian Chem. J.* **10L4** 19–30 in Russian
[52] Cirillo C, Ilyina E A and Attanasio C 2011 Static and dynamic properties of the vortex lattice in superconductor/weak ferromagnet bilayers *Supercond. Sci. Technol.* **24** 024017
[53] Minhaj M S M, Meepagala S, Chen J T and Wenger L E 1994 Thickness dependence on the superconducting properties of thin Nb films *Phys. Rev.* B **49** 15235–40
[54] Strunk C, Bruyndoncx V, Moshchalkov V V, Van Haesendonck C, Bruynseraede Y and Jonckheere R 1996 Nonlocal effects in mesoscopic superconducting aluminum structures *Phys. Rev.* B **54** R12701–4(R)
[55] Maxfield B W and McLean W L 1965 Superconducting penetration depth of niobium *Phys. Rev.* **139** A1515–22
[56] Rosseel E, Puig T, Baert M, Van Bael M J, Moshchalkov V V and Bruynseraede Y 1997 Upper critical field of Pb films with an antidot lattice *Physica* C **282-7** 1567–8
[57] Berdiyorov G R, Milošević M V and Peeters F M 2006 Vortex configurations and critical parameters in superconducting thin films containing antidot arrays: Nonlinear Ginzburg-Landau theory *Phys. Rev.* B **74** 174512
[58] Golubović D S, Pogosov W V, Morelle M and Moshchalkov V V 2003 Nucleation of superconductivity in an Al mesoscopic disk with magnetic dot *Appl. Phys. Lett.* **83** 1593–5
[59] Gillijns W, Silhanek A V and Moshchalkov V V 2006 Tunable field-induced superconductivity *Phys. Rev.* B **74** 220509(R)
[60] Pannetier B, Chaussy J, Rammal R and Villegier J C 1984 Experimental Fine tuning of frustration: two-dimensional superconducting network in a magnetic field *Phys. Rev. Lett.* **53** 1845–8
[61] Moshchalkov V V, Gielen L, Strunk C, Jonckheere R, Qiu X, Van Haesendonck C and Bruynseraede Y 1995 Effect of sample topology on the critical fields of mesoscopic superconductors *Nature* **373** 319–22
[62] Berdiyorov G R, Yu S H, Xiao Z L, Peeters F M, Hua J, Imre A and Kwok W K 2009 Effect of sample geometry on the phase boundary of a mesoscopic superconducting loop *Phys. Rev.* B **80** 064511
[63] Tinkham M 1996 *Introduction to Superconductivity* (New York: McGraw-Hill)
[64] Fink H J 1969 Vortex nucleation in a superconducting slab near a second-order phase transition and excited states of the sheath near $H_{c3}$ *Phys. Rev.* **177** 732–7
[65] Otani Y, Pannetier B, Nozières J P and Givord D 1993 Magnetostatic interactions between magnetic arrays and superconducting thin films *J. Magn. Magn. Mater.* **126** 622–5
[66] Arutyunov K Yu, Golubev D S and Zaikin A D 2008 Superconductivity in one dimension *Phys. Rep.* **464** 1–70
[67] Cirillo C, Trezza M, Chiarella F, Vecchione A, Bondarenko V P, Prischepa S L and Attanasio C 2012 Quantum phase slips in superconducting Nb nanowire networks deposited on self-assembled Si templates *Appl. Phys. Lett.* **101** 172601
[68] Trezza M, Cirillo C, Sabatino P, Carapella G, Prischepa S L and Attanasio C 2013 Nonlinear current-voltage characteristics due to quantum tunneling of phase slips in superconducting Nb nanowire networks *Appl. Phys. Lett.* **103** 252601
[69] Cirillo C, Prischepa S L, Trezza M, Bondarenko V P and Attanasio C 2014 Superconducting nanowire quantum interference device based on Nb ultrathin films deposited on self-assembled porous Si templates *Nanotechnology* **25** 425205
[70] Prischepa S L, Kupriyanov M Yu, Cirillo C and Attanasio C 2014 Magnetic memory effect in type-II superconductor/ferromagnet bilayers *Supercond. Sci. Technol.* **27** 055024